Construction of Z-scheme tungsten trioxide nanosheets-nitrogen-doped carbon dots composites for the enhanced photothermal synergistic catalytic oxidation of cyclohexane

Jinhong Zhang, Jincheng Liu*, Xiaoyu Wang, Jijin Mai, Wei Zhao, Zhongxiang Ding, Yanxiong Fang

School of Chemical Engineering and Light Industry, Guangdong University of Technology, Guangzhou, China

ABSTRACT

The novel Z-scheme WO$_3$ nanosheets-carbon dots (CDs) composites were prepared by assembling carbon dots with different terminal groups of amine groups and carboxylic acid groups on the surface of WO$_3$ nanosheets. Their microtopography, structural composition, optical and electrochemical properties are further compared. The lower fluorescence intensity and interfacial resistance of WO$_3$-N-doped carbon dots (NCDs) composites indicate the efficient electron transfer between the two semiconductors. The WO$_3$-NCDs composites show the significantly improved photothermal catalysis activity of cyclohexane oxidation with the highest conversion of 7.88% and selectivity to KA oil of 98.9%. This performance is 1.2 times that of WO$_3$-carbon dots with the carboxyl groups (CCDs) composites and 1.5 times that of pure WO$_3$ nanosheets. The significantly increased catalytic performance was caused by the effective Z-scheme charge transfer between NCDs and WO$_3$, and the accelerated chain initiation of cyclohexane oxidation by the photothermal synergistic catalysis.

1. Introduction

Partial oxidation of saturated C–H bonds has been an important challenge for catalytic chemistry [1,2]. In particular, the selective oxidation of cyclohexane has attracted extensive attention because its products cyclohexanone and cyclohexanol (KA oil) are important intermediates for the production of e-caprolactam, nylon-6 and nylon-66 [3–5]. The thermally catalyzed oxidation of cyclohexane is a homogeneous or heterogeneously catalyzed reaction carried out in the liquid phase, most of which follow the free radical reaction. Some studies have reported porphyrin metal or non-metal complexes [6,7], carbon materials [8] and nano-oxides [9] for the thermal catalysis of cyclohexane to enhance the selective catalytic oxidation activity of cyclohexane. However, there are still problems such as high reaction temperature, many side reactions, easy deep oxidation, and poor product selectivity. Therefore, it is imperative to develop a new reaction process for selective oxidation of cyclohexane under mild conditions. Photocatalytic technology is a green economy method that can effectively utilize solar energy and cheap oxygen to oxidize cyclohexane under mild conditions. The photocatalytic process involves the generation of photogenerated electrons and holes under illumination, followed by migration or recombination, and the photogenerated electrons and holes that eventually migrate to the surface react with the substances adsorbed on the surface [10,11], which is greatly different from the simple adsorption process of organic molecules on the surface of nanomaterials caused by chemical interaction and van der Waals force, and the photolysis reaction of chemical bond disconnection when the photon energy is greater than the chemical bond energy of organic pollutants. The design of a suitable photocatalyst by regulating the energy level structure for adjusting the type of active radicals to achieve high selectivity for cyclohexane oxidation under mild conditions has also been reported [12–17]. However, the lower efficiency of photocatalysis results in a long reaction time to achieve high conversion, so it is necessary to further increase the photocatalytic activity and conversion.

Photothermal synergistic catalysis can achieves high selectivity and high conversion by combining the advantages of the above two catalytic methods, achieving better performance than photocatalysis or thermal catalysis alone. The valence band generated by the semiconductor under photoexcitation can activate cyclohexane to shorten the induction period of thermal catalysis, and the photothermal effect of the semiconductor can convert light into heat, providing thermal catalyzed energy [18]. Constructing high-efficiency photothermal

synergistic catalyst is the key to improve photothermal synergistic catalytic activity. This requires the catalyst to have a strong light absorption capacity, a good charge separation transmission effect and a strong photothermal effect, and also requires a good thermal catalytic activity. Therefore, it is necessary to develop a new type of high-activity, high-selectivity, and high-stability photothermal catalyst for the study of cyclohexane oxidation.

Tungsten trioxide (WO_3) is a promising photocatalyst that responds to visible light due to its narrow band gap (~2.7 eV), high photoelectric conversion efficiency, non-toxicity and resilience to photo corrosion [19,20]. It has a extensive application in the photocatalytic oxidation because of its strong hole oxidizing ability, which is caused by a more positive valence band (VB) potential [21,22]. However, the utilization of only a portion of the visible light, insufficient conduction band (CB) potential and high recombination of photogenerated electron-hole pairs limit the further application of WO_3 [23,24].

As a new class of carbon nanomaterials, carbon quantum dots with dimensions below 10 nm possess a carbonaceous core rich in hydroxyl groups and carboxyl groups [25]. Carbon dots have received great attention due to its low toxicity, unique up-conversion fluorescence characteristics, excellent electron transfer and reservoir capabilities [26,27]. Therefore, recent studies have reported improving the photocatalytic activity in the hydrogen generation and the degradation of organic pollutants by constructing the heterostructures of WO_3 and carbon dots [28–31]. However, few studies have reported the effect of the combination method of carbon dots and WO_3 on catalytic performance. Moreover, it has been reported that N-doping can significantly improve the optical and electrical properties of carbon dots because nitrogen can alter the work function of carbon and induce the charge delocalization [32,34]. At present, most of the literature indicates that N-doped carbon quantum dots (NCDs) can greatly improve the photocatalytic performance of the host catalyst [35–38], but NCDs modified WO_3 has not been reported. Furthermore, the binding mode effect of WO_3 and carbon dots with different terminal functional groups on the photothermal catalytic performance of cyclohexane oxidation is worthy of investigation.

Here, WO_3-NCDs and WO_3 − CCDs complexes were prepared by the solvothermal methods. The composition, microstructure, crystal structure, optical and electrochemical properties of WO_3-carbon dots composites were systematically analyzed by various characterizations. The catalytic activity was evaluated by photothermal synergistic catalytic oxidation of cyclohexane with dry air as an oxidizing agent under solar light irradiation. ESR and the capture experiments of reactive species confirm that the WO_3-NCDs composite is an all-solid direct Z-scheme heterojunction, which greatly improves the separation efficiency of photogenerated electrons and holes. Subsequently, a possible mechanism of photothermal catalytic cyclohexane oxidation was proposed. Our work presents new insights that help design high-efficiency Z-scheme photothermal catalysts for cyclohexane oxidation.

2. Experimental part

2.1. Materials

Yellow tungstic acid (H_2WO_4, 99%), sodium hydroxide (NaOH, 99%), urea (99%), nitric acid, acetic acid (absolute), acetone, ethanol (absolute), oleylamine (OA, 99%) and cyclohexane (CyH, 99.5%) were purchased from Aladdin company. Citric acid (CA, 99.5%) and 6-aminohexanoic acid (AHA, 99%) were purchased from Alfa Aesar Chemical company. And deionized (DI) water was produced from Millipore-Q water purification system.

2.2. Synthesis of WO_3 nanosheets, Carbon Dots with terminal carboxyl acid and amine groups (CCDs, NCDs)

The exfoliated WO_3 nanosheets were prepared by an acetic acid-assisted intercalation stripping procedure as reported in our earlier work [17]. The acetic acid acts as an intercalant and oleylamine is used for stripping. Briefly, 200 mg of yellow tungstic acid and 3 mL of acetic acid were slowly added into 30 mL of oleylamine, the mixture was sonicated for 1 h and then transferred into a 50 mL Teflon-lined autoclave. The mixture was under a hydrothermal process at 140℃ for 12 hs. The exfoliated WO_3 nanosheets was purified twice with ethanol, and stirring in a 5 mol L^{-1} HNO_3 solution for 72 h to remove oleylamine ligands. The final WO_3 nanosheets were obtained and dispersed in ethanol for further application.

The CCDs were prepared by a pyrolysis method in our previously work [39]. Typically, 2 g 6-aminohexanoic acid and 500 mg NaOH dissolved in 20 mL DI water and stirred for 1 h. The 6-aminohexanoic sodium was obtained by vacuum-drying the mixed solution and washed twice with ethanol. Then 1 g citric acid and the 6-aminohexanoic sodium dissolved in 5 mL DI water and stirred for 1 h again. After drying the mixture at 180 ℃, the residue was sintered at 300 ℃ for 2 hs. The sinter was washed with an excess of acetone, and then the brown precipitate obtained by centrifugation was dissolved in DI water. The CCDs precipitate was collected by acidification with 5 mL of HNO_3 and then dispersed in ethanol.

The NCDs were synthesized by a hydrothermal process. 3 g of urea and 3 g of citric acid were dissolved in 10 mL of DI water and magnetically stirred for 30 min. Then the mixture was transferred into a 50 mL Teflon-lined autoclave and placed in an oven at 180 ℃ for 12 hs. After cooling, the reaction product was placed into a dialysis membrane (MwCO 1000) and purified by dialysis for 48 h. Finally, the NCDs aqueous solution was obtained by concentrating the dialysate and used for the further applications.

2.3. Synthesis of WO_3-NCDs and WO_3-CCDs

100 mg of WO_3 nanosheets were dispersed in 20 mL of absolute ethanol and sonicated for 20 min. Then a certain amount of NCDs solution and CCDs solution were added into the mixture. After sonication for 30 min, the mixture was transferred to a 50 mL Teflon-lined autoclave, and a solvothermal reaction was carried out at 120 ℃ for 4 hs. The reaction product was centrifuged and washed twice with ethanol. The final WO_3-NCDs composite and WO_3-CCDscomposite were vacuum-dried and stored for the further applications.

2.4. Characterization

The morphology and crystal structure of the prepared samples were characterized by transmission electron microscopy (TEM) and high resolution electron microscopy (HRTEM, 200 kV FEI-Talos F200S). An X-ray diffraction (XRD) pattern was obtained by an X-ray diffractometer using Cu Kα radiation (Bruker D8, Germany). The UV–vis spectrum (UV–vis) was measured using a UV–vis spectrophotometer (UV2450, Shimadzu, Japan), while the photoluminescence (PL) spectrum test was performed on a FluoroMax-4Fluorescence spectrophotometer at room temperature. Raman spectra were recorded using a Horiba JobinYvon Lab RAM HR 800 Raman spectrometer with a 633 nm laser. The FT-IR spectra were obtained using a Fourier transform infrared spectrometer (Thermofisher, Nicolet 6700). X-ray photoelectron spectroscopy (XPS) and ultraviolet photoelectron spectroscopy (UPS) were performed on an Escalab 250Xi spectrometer with a monochromic AlKα source. Thermogravimetric analysis (TGA) was conducted under dry air by a STA409PC thermogravimetric analyzer. Electron paramagnetic resonance (EPR) spectroscopy was performed on a Bruker EMX plus EPR spectrometer using 5,5-dimethyl-1-pyrroline N-oxide (DMPO) as a spin capture reagent. The photoelectrochemical (PEC) properties of the prepared samples were investigated by an electrochemical instrument (Autolab PGSTAT302 N, Switzerland) with a standard three-electrode system. The Pt line was used as a counter electrode, and the Ag/AgCl electrode was used as a reference electrode, respectively. A sample

attached to the glassy carbon electrode was used as a working electrode, and a $0.5\,mol\,L^{-1}$ Na_2SO_4 solution was used as the electrolyte solution.

2.5. Photothermal catalytic experiments

20 mg of catalyst was dispersed in 5 mL of acetone by stirring. Then 10 mL of cyclohexane was added into the mixture and sonicated for 30 min to obtain a homogeneous suspension. The mixture was then transferred into a photothermal catalytic reactor (CEL-HPR1007, Beijing Education Au-light Co., Ltd.) and a 300 W Xe lamp was used as a light source. Before the reaction, 1.5 MPa of dry air was injected into the reactor as an oxidant. The photothermal catalytic experiment was carried out at 120 °C for 8 hs under simulated sunlight irradiation. After the reaction, the product was centrifuged, and the supernatant was used for analysis by gas chromatography (GC, Agilent-7820A).

3. Results and discussion

3.1. Synthesis and characterization of photothermal catalysts

The microscopic information of carbon dots, WO_3, WO_3-CCDs and WO_3-NCDs samples were obtained from the TEM observation. The TEM images of the prepared carbon dots are shown in Fig. S1and the sizes of the CCDs and NCDs are around 5 nm. Oversized carbon dots are removed through dialysis process (MwCO 1000dialysis membrane) to eliminate the effects of different sizes. As can be seen from Fig. 1a, the prepared WO_3 is a sheet-like structure with a length of about 400 nm and a smooth surface. Due to its pliable and thin layer structure, wrinkles can also be observed. After loading carbon dots, the WO_3-CCDs and WO_3-NCDs composites maintain the two-dimensional nanosheet structure with rougher and thicker surface, indicating the combination with CCDs and NCDs (Fig. 1b and c) doesn't change the morphology of WO_3 nanosheets. The AFM images show that the thickness of the pure WO_3 nanosheet is about 2.8 nm, and the thickness becomes about 14.4 nm after loading the CCDs (Fig. S2). And the thickness of WO_3-NCDs composite is close to 16.5 nm. From their HRTEM images in Fig. 1d and e, it can be observed that WO_3 has good crystallity with the lattice spacing of 0.347 nm, which is corresponding well to the (111) crystal plane of orthorhombic WO_3 (JCPDS No. 84-0886). On the surface of WO_3, the spacing between the lattice fringes of 0.321 nm was observed for both WO_3-CCDs and WO_3-NCDs samples, which stands for the (002) plane of graphitic carbon [40]. The energy dispersive X-ray spectrometry (EDS) and element mapping of the prepared composites are shown in Fig. S3 and S4. The uniform color and gloss indicate that the elements are uniformly distributed, and it is apparent that the N element is present in WO_3-NCDs and not in WO_3-CCDs. The above analysis indicates that CCDs and NCDs are well combined with WO_3 sheets without obviously changing the morphology of WO_3. The weight ratio of carbon dots in the composites was confirmed by TGA analysis. Fig. 1f shows the TGA curves for WO_3-CCDs and WO_3-NCDs composites. The weight loss from 100 to 500 °C is caused by the decomposition of carbon dots [41], and WO_3 is the residual solid. Calculated from the weight loss percentage, the weight ratios of carbon dots in the WO_3-CCDs and WO_3-NCDs composites are about 9.0% and 9.3%.

The crystalline structures of the prepared samples were analyzed by the XRD patterns. As shown in Fig. 2, WO_3 shows strong diffraction peaks at 12.7°, 23.6°, 24.0°, 25.6°, 26.9° and 27.3°, indicating that the prepared WO_3 nanosheets were monoclinic (JCPDS No. 18-1420). And the main diffraction peaks of WO_3-CCDs appear at 16.5° and 25.6°, respectively belonging to the (020) and (111) crystal planes of orthorhombic WO_3 (JCPDS No. 84-0886), which is consistent with the observation of the TEM images. It is not difficult to find that the crystalline structure of WO_3 has changed significantly after loading carbon dots, which may be the result of the interaction between carbon dots

and WO_3. However, compared to WO_3-CCDs, WO_3-NCDs retains the (111) crystal plane diffraction peak of WO_3 at 25.6°, but the diffraction peak of the (020) plane has not been observed. Meanwhile, the other strong peaks at 8.7°, 10.5°, 17.3°, 27.7° and 35.9°are consistent with the diffraction peak of ammonium tungsten oxide (JCPDS No. 25-0045), which may be caused by the interaction between -NH_2 in NCDs and WO_3 to form ammonium tungsten oxide on the surface. In addition, no broad diffraction peaks of carbon dots were observed due to their low content and low diffraction intensity [33]. The XRD analysis indicated that the crystal structure of WO_3 could be converted under the interaction of carbon dots, and the presence of -NH_2 could form ammonium tungsten oxide with WO_3.

The chemical bonds and functional groups of the samples were investigated by FT-IR spectra. From the FT-IR spectrum of the carbon dots (Fig. S5), several peaks appearing at 3412, 1670, 1400 and $1245\,cm^{-1}$ correspond to the stretching vibrations of O−H, CO, CO and COC═ −−− [42,43]. This indicates that the surface of the carbon dots is rich in oxygen-containing groups, which facilitates the dispersion of carbon dots and the uniform bonding of carbon dots and semiconductors [26]. In addition, the FT-IR spectrum of NCDs presents strong peaks from -N-H groups at $3210\,cm^{-1}$ [44]. The FT-IR spectra of WO_3, WO_3-CCDs and WO_3-NCDscomposites are shown in Fig. 3a. All the three samples show the vibration peaks at 3412 and $1624\,cm^{-1}$from the surface adsorbed water and the vibration peakof the O−WO bond below $960\,cm^{-1}$− [21,45]. A shoulder appeared in the spectrum of WO_3-CCDs at $1005\,cm^{-1}$, which is believed to be caused by the interaction of the terminal O in the WO_3 and CCDs [46]. The absorption peaks at 3158 and $1400\,cm^{-1}$can be clearly observed in the FT-IR spectra of WO_3-NCDs, which are attributed to the vibration of NH_4^+ and C−O bonds [47]. Therefore, the FT-IR analysis reveals that CCDs and NCDs were combined with WO_3 by different chemical interaction.

The Raman spectrum was used to further confirm the formation of WO_3-CCDs and WO_3-NCDs composites (Fig. 3b). The two peaks at the Raman shifts of 261 and $325\,cm^{-1}$ are interpreted as the bending vibration of the O−WO−, while the two strong peaks at around 700 and $808\,cm^{-1}$ are designated as the stretching vibration of the O−WO− [48]. In addition, the two characteristic peaks clearly observed are the D band ($1370\,cm^{-1}$) and the G band ($1587\,cm^{-1}$), which are respectively related to the disordered and ordered carbon structures in the carbon dots [28]. This indicates that there is a certain amount of crystal structure corresponding to the carbon dots in the WO_3-carbon dots composite, which means a successful combination between them [30]. However, the intensity ratio of I_D/I_GinWO_3-NCDs was 1.18, which was higher than the value of 0.91 in WO_3-CCDs, indicating that there was more disordered carbon in WO_3-NCDsthan WO_3-CCDs [46].

XPS was used to investigate the surface chemical components to further determine the interaction between carbon dots and WO_3 nanosheets. As shown in the W 4f spectrum (Fig. 4a), there are two valence states of tungsten (W) in WO_3, WO_3-CCDs and WO_3-NCDs composites. The strong peaks at 37.76 and 35.64 eV are assigned to W^{6+}, while the shoulder peaks at 36.52 and 34.25 eV are interpreted as W^{5+} [49]. Compared with the WO_3 nanosheets, the W^{5+} peak of the WO_3-CCDs composite showed an offset of 0.1 eV, and the W^{6+} peak of the WO_3-NCDs composite also slightly converted to higher binding energy. The different changes in the binding energy of W element are caused by the different chemical interactions between carbon dots and WO_3 sheets. In the spectrum of O 1s (Fig. 4b), a broad peak at around 530.4 eV in relation to the lattice oxygen of W−O and WO═ bonds also exhibits different shifts after forming the WO_3-carbon dots composite. Then the peaks located at 532.4 and 533.0 eV are attributed to the oxygen of hydroxyl group or surface adsorbed water [46], while a new peak appears at 531.8 eV corresponding to the C−O bond from the carbon dots [37]. The high-resolution C1 s spectrum (Fig. 4c) can be fitted to three peaks at 288.8, 286.4 and 284.8 eV, which belong to the binding energy of C═O, C−O/C−N, and CC− [29]. Besides, the N 1s spectrum (Fig. 4d) present in WO_3-NCDscomposite shows two main
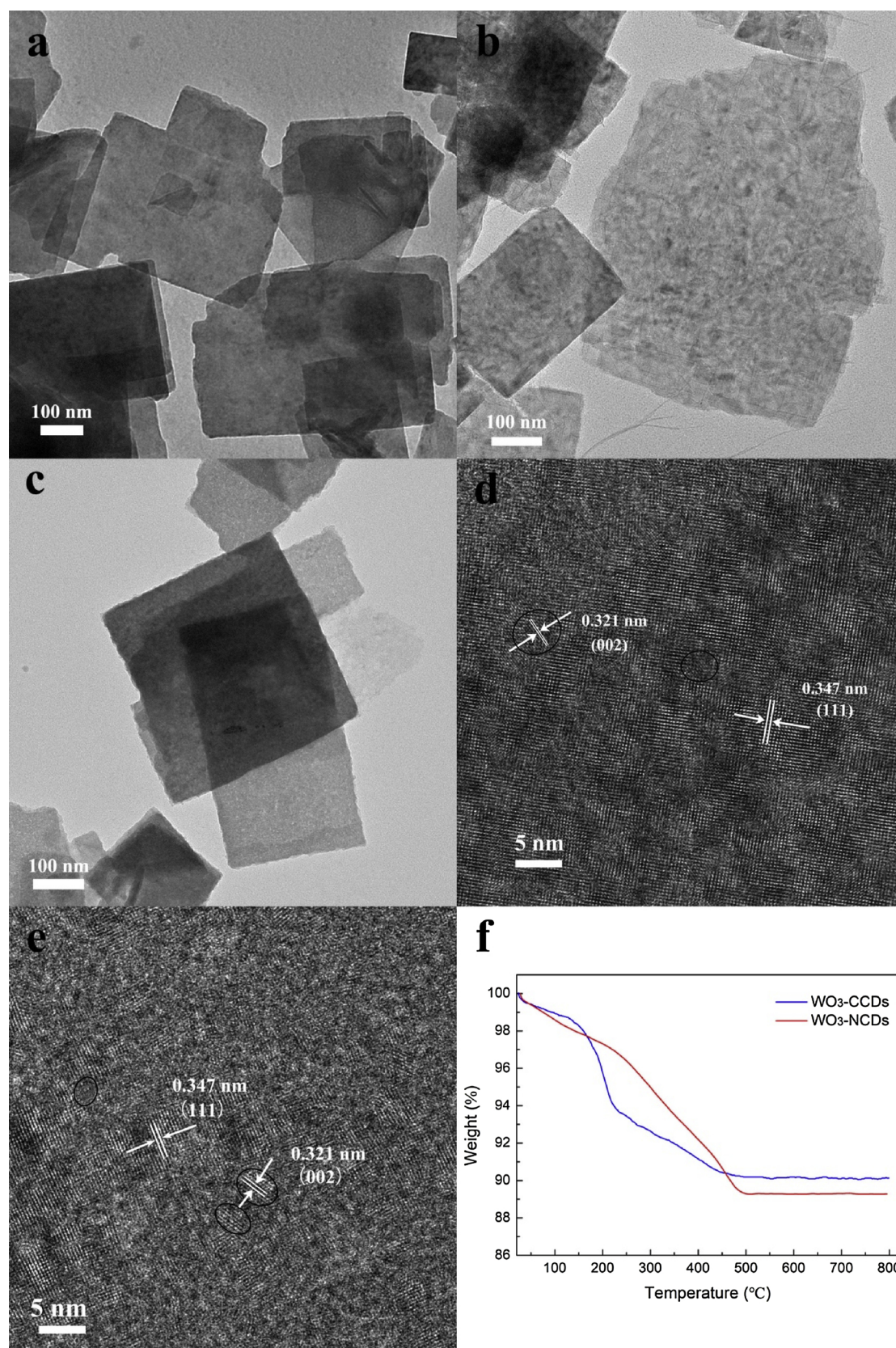
Fig. 1. TEM images of (a) WO_3 nanosheets, (b) WO_3-CCDs and (c) WO_3-NCDs composites. HRTEM images of (d) WO_3-CCDs and (e) WO_3-NCDs composites. (f) The TGA curve of WO_3-CCDs and WO_3-NCDs composites.
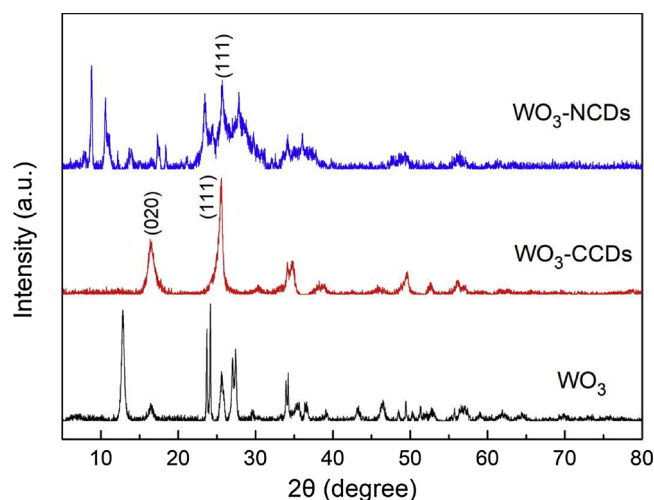
Fig. 2. XRD patterns of WO_3, WO_3-CCDs and WO_3-NCDs composites.

peaks at 401.5 and 399.6 eV, which is attributed to the nitrogen atom of N−H and CN− bonds [47]. The XPS analysis results confirm that CCDs or NCDs are well combined with WO_3 sheets, which is consistent with the above TEM, XRD, FT-IR and Raman analysis (Table 1).

Fig. 5a shows the UV–vis absorption spectra of WO_3, WO_3-CCDs and WO_3-NCDs composites. The three catalysts are capable of responding to UV and visible light, and WO_3 nanosheets have an absorption onset at around 500 nm. After compounding, the absorption edges of WO_3-CCDs and WO_3-NCDs composites are at about 525 nm and 470 nm, showing a slight red-shift and blue-shift in comparison to that of pure WO_3 nanosheets. In addition, these composites exhibited extended and enhanced visible light adsorption in the range of 500–700 nm. This indicates that the loading of carbon dots can effectively improve the absorption capacity of WO_3 nanosheets in the visible light regions, which is in agreement with other reports [31]. The optical band gap (E_g) is calculated by UV–vis absorption data according to this equation: $\alpha h\nu = A(h\nu-E_g)^{n/2}$, where α, h, and ν are the absorption coefficient, Planck constant and light frequency, and n = 1 for direct transition semiconductor [31]. As shown in Fig. S6, the calculated E_g values for WO_3, WO_3-CCDs and WO_3-NCDs composites are approximately 2.34, 2.18, and 2.14 eV, respectively. Furthermore, the CB and VB gaps (E_v) of WO_3 nanosheets are calculated to be approximately +0.88 and +3.22 eV according to the UPS spectrum (Fig. 5b).

3.2. Catalytic performance and mechanism

The time dependence of the cyclohexane oxidation conversion and the KA oil selectivity under photothermal synergetic process are shown in Fig. 6a, b and c, and the corresponding kinetic plots are shown in Fig. S7. Detailed data can be found in Table S1. After 8 h of reaction, the conversion of photocatalytic cyclohexane by the catalysts of WO_3-NCDs, WO_3-CCDs and WO_3 were 0.45%, 0.22% and 0.19%, while the conversion of thermally catalyzed cyclohexane were 6.72%, 6.66%, and 4.91%, respectively. The WO_3-NCDs has shown better both photocatalytic and thermal catalytic performance. In addition, after 8 h of photothermal synergistic catalysis, the conversion of cyclohexane with WO_3-NCDs, WO_3-CCDs and WO_3 as catalysts were 7.88%, 7.05%, and 5.31%, respectively, and the selectivity of KA oil for all the catalysts were close to 99%. This shows that WO_3-NCDs composite has better photothermal synergistic catalytic performance. Photocatalysis, thermal catalysis and photothermal catalytic reactions were also carried out (Fig. S7d) using commercial WO_3(Nanoparticles, Sigma) as a catalyst with conversions of 0.19%, 5.49% and 5.71%, respectively, which is far less than the catalytic activity of WO_3-NCDs. The results of the catalytic performance suggest that the effect of thermal catalysis is greater than that of photocatalysis, but the effect of photothermal synergistic catalysis displays better activity than their simple summation. Moreover, WO_3-NCDs exhibits better catalytic activity than WO_3-CCDs, WO_3 nanosheet and commercial WO_3 under all the catalytic processes. It is worth noting that the average reaction rate of the WO_3-NCDs catalyst in the photothermal catalytic process for 2 hs is $2.72\,h^{-1}$, which is much larger than $1.32\,h^{-1}$ for 5 hs of thermal catalysis and $0.06\,h^{-1}$ for 8 hs of photocatalysis. The photothermal catalysis shows greatly enhanced reaction speed than that under photocatalytic process and thermal catalytic process. This may be attributed to the fact that the irradiation of visible light can generate electron-hole pairs to promote the initiation of chain initiation and accelerate the catalytic process. The results of the photothermal catalytic reaction of WO_3-NCDs and WO_3-CCDs at different temperatures are shown in Fig. 6d. With the increase of reaction temperature, the cyclohexane conversion and KA oil selectivity increase from 100 to 120 °C and decreased at the temperature from 120 to 140 °C. The optimized best photothermal catalytic performance was obtained at 120 °C.This may be due to a decrease in catalyst activity at high temperature or excessive oxidation of the products. Besides, we also investigated the effect of the NCDs content on theWO₃-NCDs catalytic activity. As shown in Fig. 6e, the catalytic activity increases rapidly as the NCDs content increases and then slowly decreases. Obviously, the WO_3-NCDs composite with NCDs mass fraction of 9.3% exhibits the highest conversion (7.88%) of cyclohexane, which is 1.5 times that of WO_3 nanosheets. This indicates
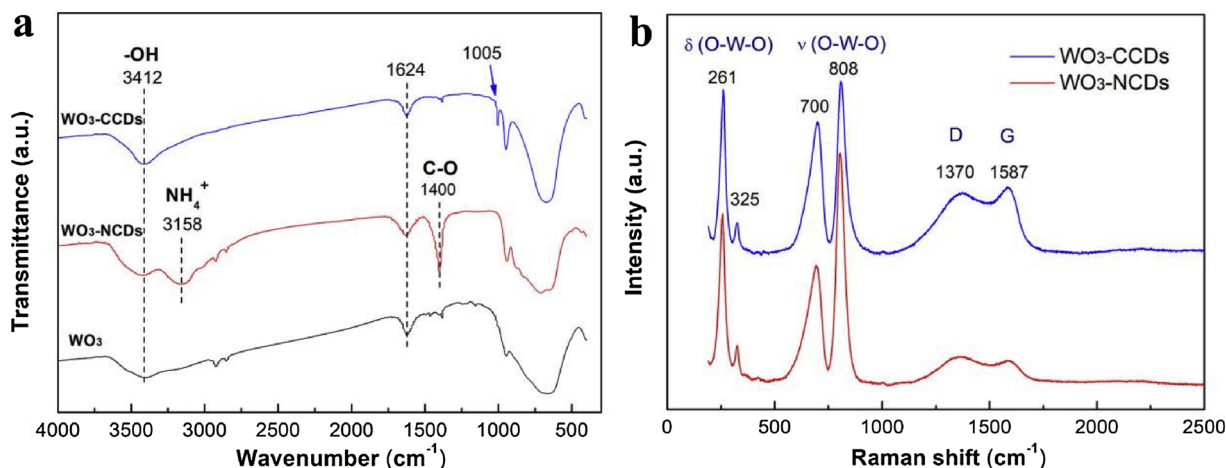

Fig. 3. (a) FT-IR and (b) Raman spectra of WO_3, WO_3-CCDs and WO_3-NCDs composites.
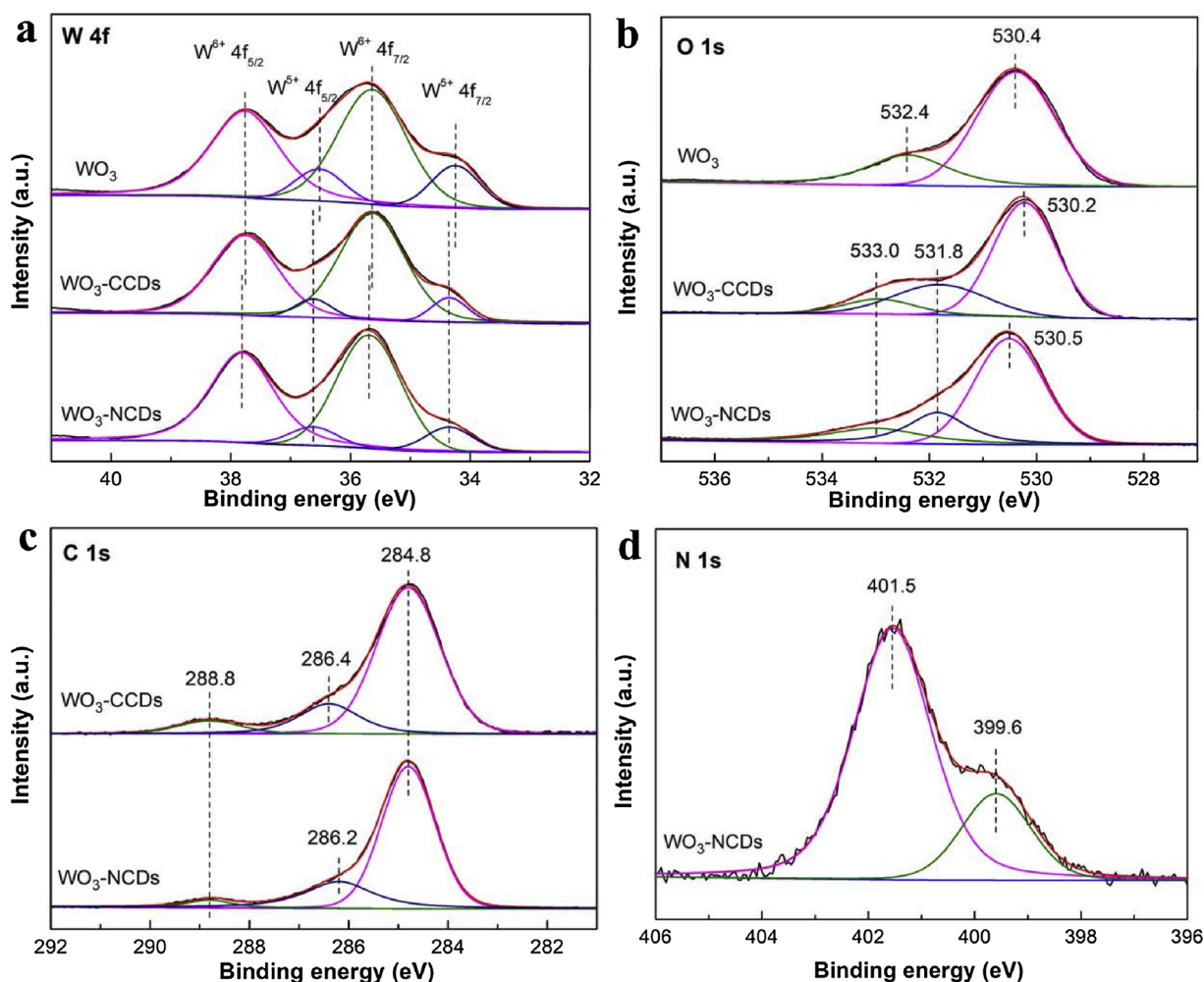
Fig. 4. XPS spectra of WO_3, WO_3-CCDs and WO_3-NCDs composites.

Table 1
Performance comparison of previous studies similar to our system.

Entry	Catalyst	Reaction condition	Oxidant	Conv. (%)	Selectivity (%)		Ref.
					K	A	
1	CFO/SiO_2-5	5 mg cat. 7 mL CyH, 145 °C, 6 h	O_2	7.4	53.1	42.3	50
2	Au/CQDs	25 mg cat. 50 mL CyH, Xe lamp, 48 h	H_2O_2	63.8	99.9		13
3	C_3N_4/Au	500 mg cat. 10 mL CyH, Xe lamp, 60 °C, 24 h	–	10.54	100	0	12
4	$(nBu4N)_4W_{10}O_{32}$	molar ratio of cat. to the CyH is 0.014, bromine tungstene lamp, 27 °C, 12 h	O_2	8.1	64.3	35.7	51
5	polytriazine imide	150 mg cat. 10 mL CyH, Xe lamp, 60 °C, 48 h	Air	5.81	99.9	0	15
6	$Fe_{0.2}Ti_{0.02}$–SBA	30 mg cat. 2 mL CyH, 300 W solar simulator, 48 h	O_2	2.0	99		52
7	TiO_2/ rGO	20 mg cat. 5 mL CyH, Xe lamp, 25 °C, 12 h	O_2	0.1	83	5.2	5
8	NH_2-MIL125/TiO_2	50 mg cat. 10 mL CyH, Xe lamp, 25 °C, 5 h	O_2	0.74	63	36	53
9	WO_3-Ag	mass ratio of cat. to the CyH is 0.25 %, Xe lamp, 25 °C, 48 h	TBHP	40.2	97		17
10	Bis(8-quinolinolato) oxovanadium (IV)	molar ratio of cat. to the CyH is 0.01, bromine tungsten lamp, 0.1 mL HCl, 30 °C, 10 h	O_2	18.66	79.4	16	54
11	$BiVO_4$	50 mg cat. 5 mmolCyH, bromine tungsten lamp, 0.1 mL HCl, 30 °C, 8 h	O_2	15.5	71	24	55
12	$VOCl_2$	1 mmol cat. 5 mL CyH, Xe lamp, 30 °C, 4 h	O_2	17.8	64.4	34.4	56
13	WO_3-NCDs	20 mg cat. 10 mL CyH, Xe lamp, 120 °C, 8h	Air	7.88	42.3	46.5	This work

that loading an appropriate amount of NCDs can significantly improve the photothermal catalytic cyclohexane oxidation performance of WO_3 nanosheets. In order to investigate the stability of the catalyst, the photothermal catalytic oxidation of cyclohexane was carried out for 5 cycles (Fig. 6f). After 5 cycling reaction, there was no significant change

in conversion and selectivity, indicating that the catalyst has excellent long-term catalytic stability. The AFM image shows no significant change in the thickness of NC and CC after the catalytic reaction (Fig. S2). Furthermore, in the TEM, XRD and FTIR spectra of Fig. S8, the morphology, crystal structure and chemical composition of WO_3-NCDs
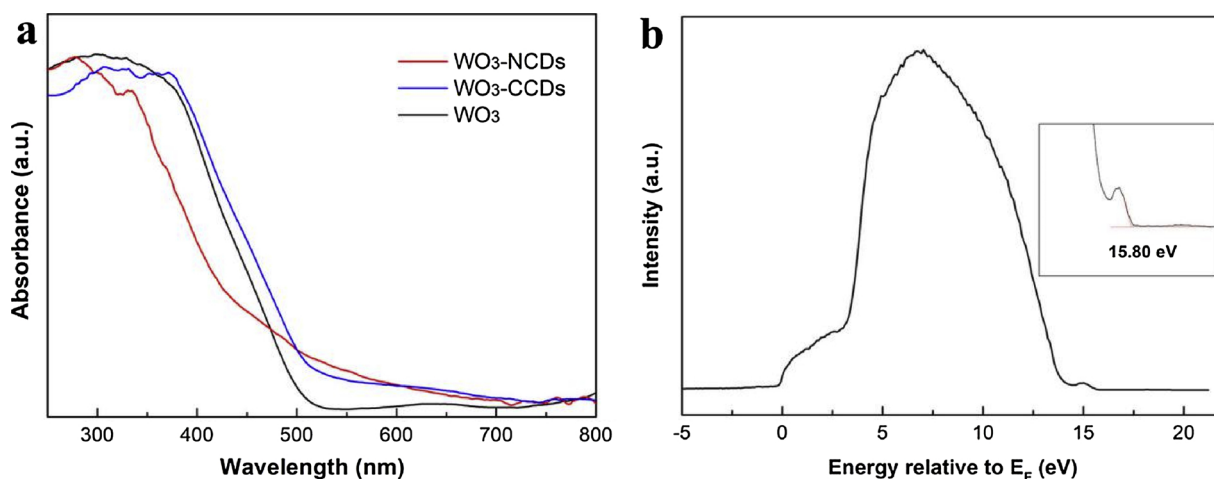
Fig. 5. (a) UV–vis absorption spectra and (b) UPS spectra of WO_3, WO_3-CCDs and WO_3-NCDs composites.

and WO_3-CCDs composites did not change significantly after 8 h of photothermal catalytic reaction, indicating good structural stability.

The catalytic performance of the prepared catalyst was compared with the reported studies with similar catalytic systems [5,12,13,15,17,50–56]. The reaction was carried out under solar light illumination and had better performance at lower temperatures than Entry 1. Compared to peroxide and pure O_2 as an oxidant, the use of air as an oxidant appears to be milder and more economical. Moreover, the development of low-cost non-precious metal catalysts has a better prospect. Many studies have shown that the addition of HCl to the reaction system can significantly increase the conversion of cyclohexane. However, this will introduce a new by-product of chlorocyclohexane, which will cause a decrease in the selectivity of KA oil. The developed WO_3-NCDs composite catalyzes the oxidation of cyclohexane with air as an oxidant under light irradiation and 120 °C, showing an ideal conversion and high selectivity [50–56].

PL spectra is used to investigate the charge transfer of catalysts, while weak fluorescence intensity is indicative of lower recombination rates of photogenerated electrons and hole pairs [57]. The emission peaks of WO_3, WO_3-CCDs and WO_3-NCDs composites appear at 400˜600 nm at the excitation of 320 nm in Fig. 7a. It can be observed that the PL intensity is significantly reduced after the carbon dots are anchored to the surface of WO_3. This may be because that the photogenerated electrons of WO_3 are transferred to the carbon dots and quenched, which the carbon dots act as an electron acceptor. Then the WO_3-NCDs composite is the lowest fluorescence intensity among them, indicating a lower recombination rate of photogenerated electrons and hole pairs. In addition, the transfer efficiency of photogenerated electrons in the interface region is further investigated by transient photocurrent response and electrochemical impedance spectroscopy (EIS) measurement [58]. The photocurrent response curves of WO_3, WO_3-CCDs and WO_3-NCDs composites are shown in Fig. 7b. The WO_3-NCDs composite displays the highest photocurrent intensity under solar light irradiation, which is about 1.5 times of WO_3-CCDs and ˜15.2 times of WO_3. This indicates that WO_3-NCDs composite has a higher charge separation rate under solar light irradiation. The semicircle arc radius exhibited in the EIS spectrum (Fig. 7c) follows the order: $WO_3 > WO_3-CCDs > WO_3$-NCDs. This suggests that WO_3-NCDs composite has a smaller resistance at the interface region, facilitating faster charge transfer at the interface. The PL and electrochemical analysis indicated that NCDs can act as a good electron acceptor and transporter, which makes WO_3-NCDs have better charge separation and transfer ability under solar light irradiation. This results in a higher

photocatalytic performance of WO_3-NCDs composites, which is consistent with the performance experiment results.

In order to investigate the effects of reactive species in the oxidation of cyclohexane, the reactive species trapping experiments were carried out with triethanolamine (TEAO, a hole scavenger), benzoquinone (BQ, a O_2-radical scavenger) and *tert*-butanol (TBA, a OH radical scavenger) [12]. The results of the catalytic performance after trapping are shown in Fig. 8. The cyclohexane conversion decreased slightly after the addition of TEOA, indicating that the hole may not be the main reactive species in the catalytic process. After O_2- radical was removed by BQ, the conversion of cyclohexane decreased by nearly 1.3%, implying that ·O_2-radical has a certain effect on the oxidation of cyclohexane. Moreover, the catalytic activity of oxidized cyclohexane was significantly decreased from 7.88% to 3.98% in 8 h when TBA was introduced to trap OH radical. This phenomenon represents that ·OH radical has a great influence on the oxidation of cyclohexane. Therefore, the reactive species trapping experiments demonstrate that ·OH and ·O_2- radical are the main reactive species in the photothermal catalytic oxidation of cyclohexane, which is similar to the results reported by Zhang and his colleagues [15].

The EPR test was performed to detect the O_{2-} and ·OH radical produced by the catalyst under photoexcitation in the solution. Fig. 9a shows the signal of DMPO-O_2-adduct obtained by simulating photocatalytic oxidation of cyclohexane in the mixture of acetone and CyH (1/2 v/v, 15 mL) with the catalyst. It is clear that strong signal intensities can be observed for WO_3-NCDs and WO_3-CCDs composites, while only very weak signals are present in WO_3 nanosheets. The same weak signal can be observed in the relevant WO_3 system [59]. Since the conduction band (CB) potential of WO_3 is more positive than the standard redox potential of O_2/O_2- (-0.33 eV, vs NHE), it is difficult for photogenerated electrons on the CB of WO_3 to single-electron reduction O_2 to form O_2-. After loading the NCDs, the electrons on the NCDs CB on the surface of the WO_3-NCDs composite have sufficient ability to reduce O_2, resulting in strong intensity of DMPO-O_2- signal. This suggests that the holes generated under photoexcitation remain on the VB of WO_3 without being transferred to the VB of the NCDs. The EPR test results suggest that the oxidation and reduction reactions occur on the valence band holes of WO_3 and the conduction band electrons of carbon dots. This demonstrates that the effective charge transfer between WO_3 and NCDs should follow the Z-scheme heterojunction mechanism rather than the Type II heterojunction mechanism. While h^+ can only react with a small amount of water present in the system to produce little OH radical, the signal intensity is so low that it is difficult to be observed in
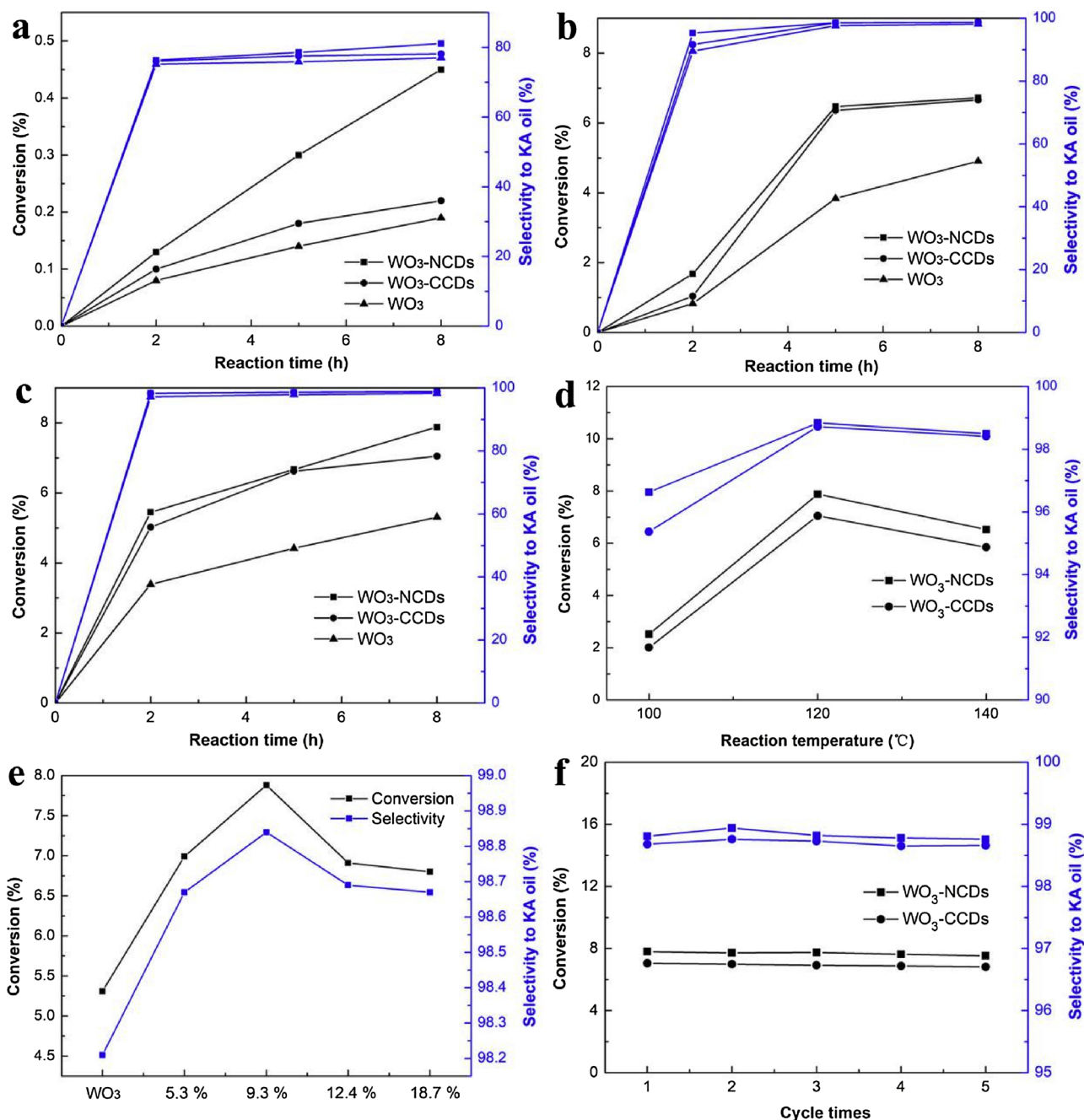
Fig. 6. The time dependence of the conversion and KA-oil selectivity under(a) photocatalytic, (b) thermal catalytic and (c) photothermal catalytic cyclohexane oxidation by 9.3% WO_3-NCDs, 9.0% WO_3−CCDs and WO_3 nanosheets. (d) The conversion and selectivity of photothermal catalytic cyclohexane oxidation at different temperatures under solar light irradiation. (e) The conversion of cyclohexane oxidation and KA-oil selectivity by WO_3 nanosheets and WO_3-NCDs composites with different NCDs contents. (f) Recyclability of photothermal catalytic cyclohexane oxidation by 9.3% WO_3-NCDs for 5 cycles.

the EPR spectrum (Fig. 9a). However, strong signal of DMPO-OH adduct can be observed in the aqueous solution (Fig. 9b). Furthermore, the signal intensity of the DMPO-OH adduct obtained with WO_3-NCDs composite in aqueous solution is slightly weaker than that of the WO_3 nanosheet. This may be due to the fact that WO_3 acts as the primary OH radical generating site, while the loading of the NCDs reduces the active sites of WO_3 with H_2O resulting in a slightly decrease in OH radical production. Because the conversion of cyclohexane by photothermal catalytic oxidation is greatly reduced by the removal of OH radical, we speculate that OH radical is mainly formed through the chain

propagation process in thermal catalytic. The trapping experiment and EPR analysis indicate that the O_{2^-} and $_{O}H$ radicals are the main reactive species produced during the photocatalytic oxidation of cyclohexane.

Based on the above analysis, we propose a possible mechanism for WO_3-NCDs composites catalytic oxidation of cyclohexane. The VB and CB values of WO_3 nanosheets are $+3.22$ and $+0.88$ eV according to the analysis, while the VB and CB values for NCDs are about $+2.11$ and -0.25 eV obtained from related literature [60]. As shown in Fig. 10, the NCDs are loaded on the surface of WO_3 and constitute a Z-scheme heterostructure. Under the illumination of sunlight, WO_3 and NCDs are
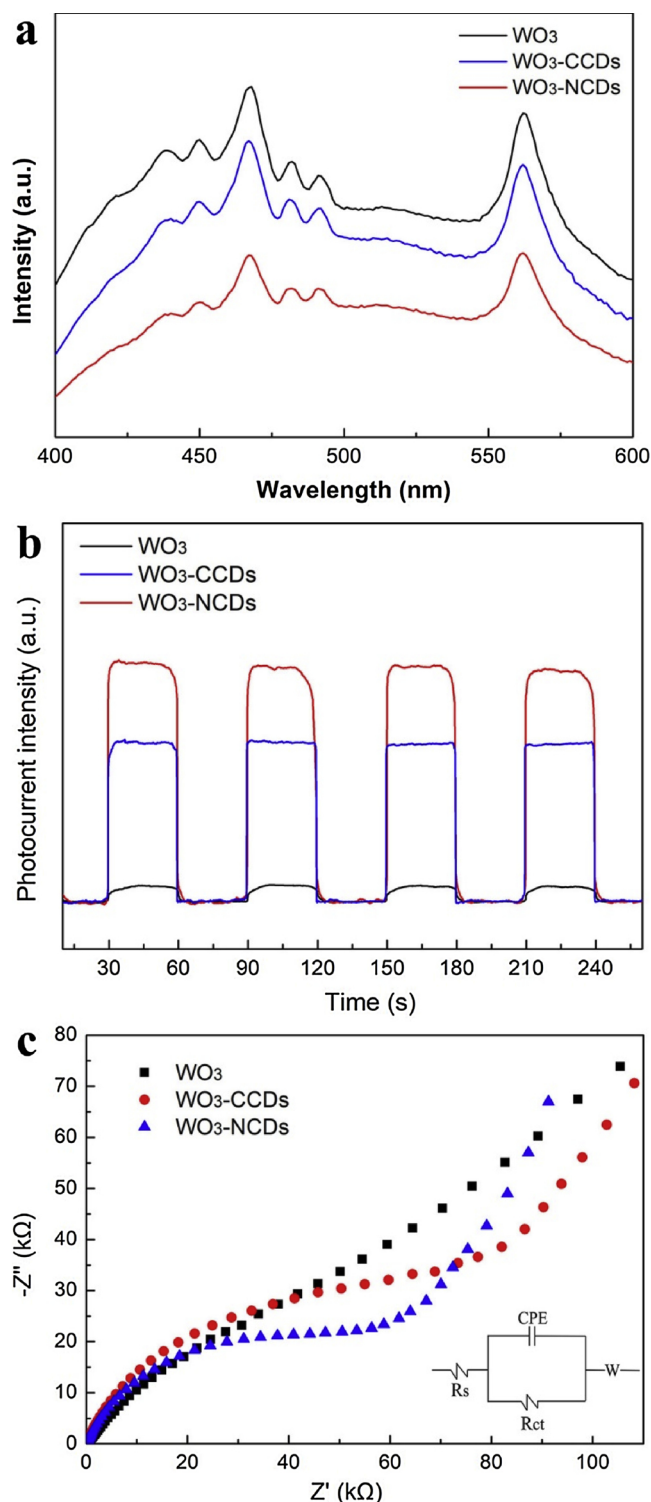
a PL spectra with WO₃, WO₃-CCDs, WO₃-NCDs

Fig. 8. Photothermal catalysis activities of WO_3-CCDs and WO_3-NCDs composites in reactive species trapping experiments with the reactive species scavengers of TEOA, BQ and TBA.

chain propagation reactions by the thermal catalytic process to finally form cyclohexanone and cyclohexanol. The Z-scheme charge transfer mechanism effectively promotes the separation of photogenerated electrons and hole pairs, and greatly prolongs the lifetime of photogenerated electrons on the CB of NCDs and holes on the VB of WO_3. Therefore, the formation of a Z-scheme heterostructure on the WO_3 nanosheet by the loaded NCDs can greatly improve the photocatalytic redox performance and contribute to the oxidation of cyclohexane. In addition, the separation and migration of photogenerated electrons and holes are rapidly induced by solar light irradiation, and the reactive species can be generated in a short time. This accelerates the chain initiation of cyclohexane oxidation, allowing photothermal synergistic catalysis to have a higher cyclohexane conversion than thermal catalysis.

4. Conclusions

In summary, the Z-scheme composite catalysts of WO_3 nanosheets and carbon dots with different functional groups were prepared for a comparative study in the photothermal catalytic oxidation of cyclohexane. TEM and XRD results demonstrated that carbon dots with different functional groups were successfully anchored on the surface of WO_3 nanosheets. The crystal structure of WO_3 could be converted under the interaction of carbon dots, and the combination of NCDs and WO_3 forms tungsten ammonium oxide. FT-IR and XPS further demonstrate that NCDs are assembled on WO_3 nanosheets by terminal amine groups to form tungsten ammonium oxide, while CCDs are assembled on WO_3 nanosheets by carboxyl groups. The WO_3-NCDs exhibits better catalytic activity than WO_3-CCDs both in photocatalysis, thermal catalysis and photothermal synergistic catalysis. The WO_3-NCDs composites significantly improved the photothermal catalysis activity of cyclohexane oxidation, and achieved the highest conversion of 7.88% at the NCDs weight percent of 9.3%. This performance is 1.5 times of that by pure WO_3 nanosheets and 1.2 times of that by WO_3-CCDs composites. The Z-scheme charge transfer mechanism between NCDs and WO_3 is determined by PL, PEC, UPS, and EPR analysis, which effectively inhibits the recombination of photogenerated electrons and holes, and improves the redox ability of the photocatalyst. This mechanism prolongs the lifetime of photogenerated electrons on the CB of NCDs to generate O_2-radical, which is one of the main reactive species in the oxidation of cyclohexane. Our research and finding is interesting and helpful for the efficient catalyst design for the catalytic oxidation of cyclohexane.

Fig. 7. (a) PL spectra, (b) transient photocurrent responses and (c) EIS Nyquist plots of WO_3, WO_3-CCDs and WO_3-NCDs composites.

simultaneously excited, and the photogenerated electrons transition from the VB to the CB. Then the electrons on the CB of WO_3 are transferred to the NCDs and quenched with holes on the VB of NCDs through the hetero-interface. The photogenerated electrons on the CB of NCDs have a strong reducing ability and reduce O_2 to O_2-radical. Correspondingly, the holes in the VB of WO_3 oxidize H_2O to OH or directly oxidize cyclohexane to obtain cyclohexyl radical (Cy). Under the above reactive species, cyclohexane undergoes a series of radical
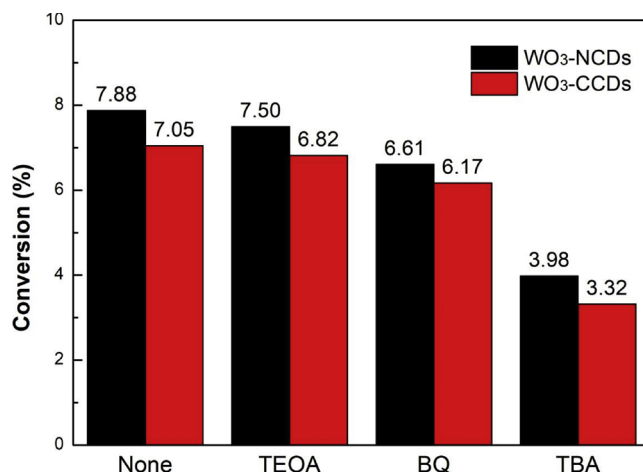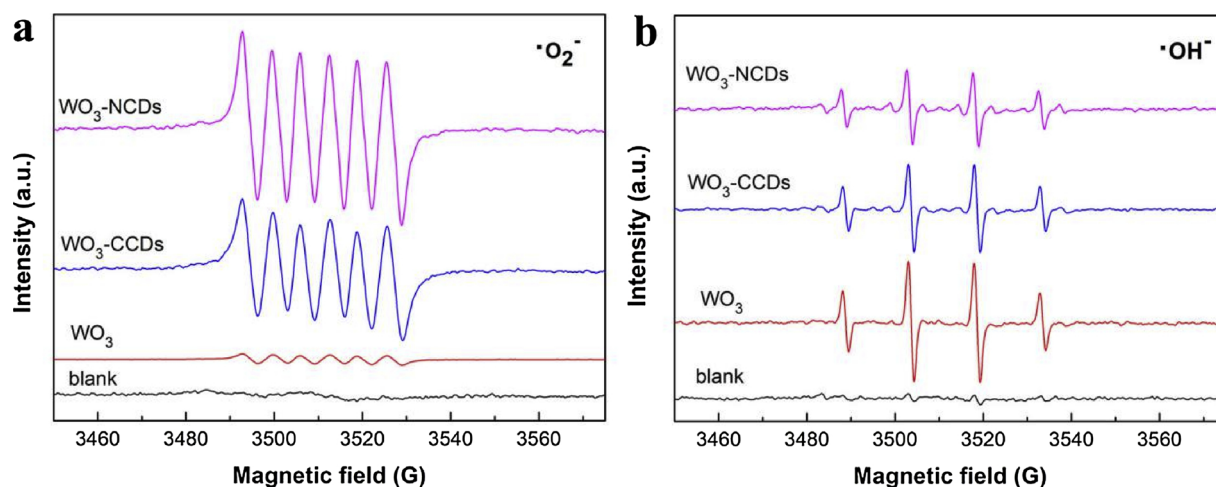
Fig. 9. The ESR signals of the DMPO-O_2^- adducts in acetone/CyH (1/2 v/v, 15 mL) mixture and the adducts in water with DMPO as the spin-trap reagent under solar light irradiation (20 mg catalyst, 0.25 mM DMPO, 5 min of irradiation).
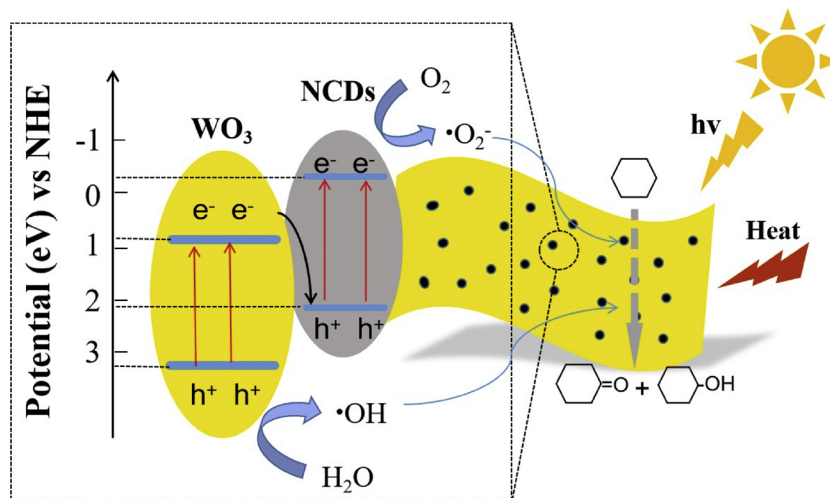

Fig. 10. The possible schematic diagram of photothermal synergistic catalytic cyclohexane oxidation under solar light irradiation.

Declaration of Competing Interest

The authors declare that they have no known competing financial interests or personal relationships that could have appeared to influence the work reported in this paper.

Acknowledgments

Appendix A. Supplementary data

Supplementary material related to this article can be found, in the online version, at doi:https://doi.org/10.1016/j.apcatb.2019.118063.

References

[1] T.J. Collins, A.D. Ryabov, Targeting of high-valent iron-TAML activators at hydrocarbons and beyond, Chem. Rev. 117 (2017) 9140–9162, https://doi.org/10. 1021/acs.chemrev.7b00034.

[2] Y. Xiao, J. Liu, K. Xie, W. Wang, W. Fang, Aerobic oxidation of cyclohexane catalyzed by graphene oxide: effects of surface structure and functionalization, Mol. Catal. 431 (2017) 1–8, https://doi.org/10.1016/j.mcat.2017.01.020.

[3] U. Schuchardt, D. Cardoso, R. Sercheli, R. Pereira, R.S. de Cruz, M.C. Guerreiro, D. Mandelli, E.V. Spinace, E.L. Fires, Cyclohexane oxidation continues to be a challenge, Appl. Catal. A Gen. 211 (2001) 1–17, https://doi.org/10.1016/S0926-860X(01)00472-0.

[4] Y. Shiraishi, Y. Sugano, S. Ichikawa, T. Hirai, Visible light-induced partial oxidation of cyclohexane on WO₃ loaded with Pt nanoparticles, Catal. Sci. Technol. 2 (2012) 400–405, https://doi.org/10.1039/c1cy00331c.

[5] Y. Shiraishi, S. Shiota, H. Hirakawa, S. Tanaka, S. Ichikawa, T. Hirai, Titanium Dioxide/Reduced graphene oxide hybrid photocatalysts for efficient and selective partial oxidation of cyclohexane, ACS Catal. 7 (2017) 293–300, https://doi.org/10. 1021/acscatal.6b02611.

[6] K. Machado, S. Mukhopadhyay, G.S. Mishra, Nanoparticles silica anchored Cu-(II) and V-(IV) scorpionate complexes for selective catalysis of cyclohexane oxidation, J. Mol. Catal. A Chem. 400 (2015) 139–146, https://doi.org/10.1016/j.molcata.2015. 01.026.

[7] G. Huang, Y. Liu, J.L. Cai, X.F. Chen, S.K. Zhao, Y.A. Guo, S.J. Wei, X. Li, Heterogeneous biomimetic catalysis using iron porphyrin for cyclohexane oxidation promoted by chitosan, Appl. Surf. Sci. 402 (2017) 436–443, https://doi.org/10. 1016/j.apsusc.2017.01.082.

[8] H. Yu, F. Peng, J. Tan, X. Hu, H. Wang, J. Yang, W. Zheng, Selective catalysis of the aerobic oxidation of cyclohexane in the liquid phase by carbon nanotubes, Angew. Chemie Int. Ed. English 50 (2011) 3978–3982, https://doi.org/10.1002/anie. 201007932.

[9] M. Wu, W. Zhan, Y. Guo, Y. Guo, Y. Wang, L. Wang, G. Lu, An effective Mn-Co mixed oxide catalyst for the solvent-free selective oxidation of cyclohexane with

molecular oxygen, Appl. Catal. A-Gen. 523 (2016) 97–106, https://doi.org/10.1016/j.apcata.2016.06.001.

[10] K. Dashtian, M. Ghaedi, H. Shirinazadeh, S. Hajati, S. Shahbazi, Achieving enhanced blue-light-driven photocatalysis using nanosword-like VO2/CuWO4 type II n–n heterojunction, Chem. Eng. J. 339 (2018) 189–203, https://doi.org/10.1016/j.cej.2018.01.107.

[11] M.H. Barzegar, M. Ghaedi, V.M. Avargani, M.M. Sabzehmeidani, F. Sadeghfar, R. Jannesar, Electrochemical synthesis and efficient photocatalytic degradation of azo dye alizarin yellow R by Cu/CuOnanorods under visible LED light irradiation using experimental design methodology, Polyhedron 158 (2019) 506–514, https://doi.org/10.1016/j.poly.2018.10.040.

[12] J. Liu, Y. Yang, N. Liu, Y. Liu, H. Huang, Z. Kang, Total photocatalysisconversion from cyclohexane to cyclohexanone by C3N4/Au nanocomposites, Green Chem. 16 (2014) 4559–4565, https://doi.org/10.1039/c4gc01126k.

[13] R. Liu, H. Huang, H. Li, Y. Liu, J. Zhong, Y. Li, S. Zhang, Z. Kang, Metal nanoparticle/carbon quantum dot composite as a photocatalyst for high-Efficiency cyclohexane oxidation, AcsCatal. 4 (2014) 328–336, https://doi.org/10.1021/cs400913h.

[14] W. Zhong, T. Qiao, J. Dai, L. Mao, Q. Xu, G. Zou, X. Liu, D.L. Yin, F. Zhao, Visible-light-responsive sulfated vanadium-doped TS-1 with hollow structure: enhanced photocatalytic activity in selective oxidation of cyclohexane, J. Catal. 330 (2015) 208–221, https://doi.org/10.1016/j.jcat.2015.06.013.

[15] Y. Zhang, L. Hu, C. Zhu, J. Liu, H. Huang, Y. Liu, Z. Kang, Air activation by a metal-free photocatalyst for "totally-green" hydrocarbon selective oxidation, Catal.Sci. Technol. 6 (2016) 7252–7258, https://doi.org/10.1039/c6cy01066k.

[16] A. Henriquez, H.D. Mansilla, A. Martinez Martinez-de La Cruz, J. Freer, D. Contreras, Selective oxofunctionalization of cyclohexane over titanium dioxide-based and bismuth oxyhalide (BiOX, X = Cl⁻, Br⁻, I⁻) photocatalysts by solar light irradiation, Appl. Catal. B-Environ. 206 (2017) 252–262, https://doi.org/10.1016/j.apcatb.2017.01.022.

[17] Y. Xiao, J. Liu, J. Mai, C. Pan, X. Cai, Y. Fang, High-performance silver nanoparticles coupled with monolayer hydrated tungsten oxide nanosheets: the structural effects in photocatalytic oxidation of cyclohexane, J. Colloid Interf. Sci. 516 (2018) 172–181, https://doi.org/10.1016/j.jcis.2018.01.057.

[18] L. Chen, J. Tang, L. Song, P. Chen, J. He, C. Au, S. Yin, Heterogeneous photocatalysis for selective oxidation of alcohols and hydrocarbons, Appl. Catal. B-Environ. 242 (2019) 379–388, https://doi.org/10.1016/j.apcatb.2018.10.025.

[19] X. An, J.C. Yu, Y. Wang, Y. Hu, X. Yu, G. Zhang, WO3 nanorods/graphene nanocomposites for high-efficiency visible-light-driven photocatalysis and NO2 gas sensing, J. Mater. Chem. 22 (2012) 8525–8531, https://doi.org/10.1039/c2jm16709c.

[20] S.S. Kalanur, Y.J. Hwang, S.Y. Chae, O.S. Joo, Facile growth of aligned WO3 nanorods on FTO substrate for enhanced photoanodic water oxidation activity, J. Mater. Chem.A. 1 (2013) 3479–3488, https://doi.org/10.1039/c3ta01175e.

[21] J. Zhang, J. Liu, W. Zhao, Z. Ding, J. Mai, Y. Fang, Facile synthesis of high quality Z-scheme W18O49 nanowire-g-C3N4photocatalyst for the enhanced visible light-driven photocatalytic hydrogen evolution, J. Alloys. Compd. 764 (2018) 1–9, https://doi.org/10.1016/j.jallcom.2018.06.045.

[22] H. Suzuki, O. Tomita, M. Higashi, R. Abe, Tungstic acids H2WO4 and H4WO5 as stable photocatalysts for water oxidation under visible light, J. Mater. Chem. A5 (2017) 10280–10288, https://doi.org/10.1039/c7ta01228d.

[23] Y. Hou, F. Zuo, A.P. Dagg, J. Liu, P. Feng, Branched WO3 nanosheet array with layered C3N4 heterojunctions and CoOx nanoparticles as a flexible photoanode for efficient photoelectrochemical water oxidation, Adv. Mater. 26 (2014) 5043–5049, https://doi.org/10.1002/adma.201401032.

[24] W. Yu, J. Chen, T. Shang, L. Chen, L. Gu, T. Peng, Direct Z-scheme g-C3N4/WO3photocatalyst with atomically defined junction for H2 production, Appl. Catal. B-Environ. 219 (2017) 693–704, https://doi.org/10.1016/j.apcatb.2017.08.018.

[25] J. Zhang, S. Yu, Carbon dots: large-scale synthesis, sensing and bioimaging, Mater Today. 19 (2016) 382–393, https://doi.org/10.1016/j.mattod.2015.11.008.

[26] H. Li, Z. Kang, Y. Liu, S. Lee, Carbon nanodots: synthesis, properties and applications, J. Mater. Chem. 22 (2012) 24230–24253, https://doi.org/10.1039/c2jm34690g.

[27] P. Roy, P. Chen, A.P. Periasamy, Y. Chen, H. Chang, Photoluminescent carbon nanodots: synthesis, physicochemical properties and analytical applications, Mater. Today 18 (2015) 447–458, https://doi.org/10.1016/j.mattod.2015.04.005.

[28] P. Yang, J. Zhao, J. Wang, B. Cao, L. Li, Z. Zhu, Construction of Z-scheme carbon nanodots/WO3 with highly enhanced photocatalytic hydrogen production, J. Mater.Chem.A. 3 (2015) 8256–8259, https://doi.org/10.1039/c5ta00657k.

[29] F. Yan, D. Kong, Y. Fu, Q. Ye, Y. Wang, L. Chen, Construction of carbon nanodots/tungsten trioxide and their visible-light sensitive photocatalytic activity, J. Colloid Interf. Sci. 466 (2016) 268–274, https://doi.org/10.1016/j.jcis.2015.12.043.

[30] J. Zhang, Y. Ma, Y. Du, H. Jiang, D. Zhou, S. Dong, Carbon nanodots/WO3 nanorods Z-scheme composites: remarkably enhanced photocatalytic performance under broad spectrum, Appl. Catal. B-Environ. 209 (2017) 253–264, https://doi.org/10.1016/j.apcatb.2017.03.017.

[31] B. Song, T. Wang, H. Sun, Q. Shao, J. Zhao, K. Song, L. Hao, L. Wang, Z. Guo, Two-step hydrothermally synthesized carbon nanodots/WO3 photocatalysts with enhanced photocatalytic performance, Dalton Trans. 46 (2017) 15769–15777, https://doi.org/10.1039/c7dt03003g.

[32] Y. Sun, Z. Zhang, A. Xie, C. Xiao, S. Li, F. Huang, Y. Shen, An ordered and porous N-doped carbon dot-sensitized Bi2O3 inverse opal with enhanced photoelectrochemical performance and photocatalytic activity, Nanoscale. 7 (2015) 13974–13980, https://doi.org/10.1039/c5nr03402g.

[33] J. Zhang, X. Zhang, S. Dong, X. Zhou, S. Dong, N-doped carbon quantum dots/TiO2 hybrid composites with enhanced visible light driven photocatalytic activity toward

[34] J. Huang, Y. Li, Y. Cao, F. peng, Y. Cao, Q. Shao, H. Liu, Z. Guo, Hexavalent chromium removal over magnetic carbon nanoadsorbents: synergistic effect of fluorine and nitrogen co-doping, J. Mater. Chem. A Mater. Energy Sustain. 6 (2018) 13062–13074, https://doi.org/10.1039/c8ta02861c.

[35] J. Di, J. Xia, M. Ji, B. Wang, X. Li, Q. Zhang, Z. Chen, H. Li, Nitrogen-Doped carbon quantum Dots/BiOBr ultrathin nanosheets: in situ strong coupling and improved molecular oxygen activation ability under solar light irradiation, ACS Sustain. Chem. Eng. 4 (2016) 136–146, https://doi.org/10.1021/acssuschemeng.5b00862.

[36] J. Di, J. Xia, X. Chen, M. Ji, S. Yin, Q. Zhang, H. Li, Tunable oxygen activation induced by oxygen defects in nitrogen doped carbon quantum dots for sustainable boosting photocatalysis, Carbon 114 (2017) 601–607, https://doi.org/10.1016/j.carbon.2016.12.030.

[37] F. Wang, P. Chen, Y. Feng, Z. Xie, Y. Liu, Y. Su, Q. Zhang, Y. Wang, K. Yao, W. Lv, G. Liu, Facile synthesis of N-doped carbon dots/g-C3N4 photocatalyst with enhanced visible-light photocatalytic activity for the degradation of indomethacin, Appl. Catal.B-Environ. 207 (2017) 103–113, https://doi.org/10.1016/j.apcatb.2017.02.024.

[38] F. Wang, Y. Wu, Y. Wang, J. Li, X. Jin, Q. Zhang, R. Li, S. Yan, H. Liu, Y. Feng, G. Liu, W. Lv, Construction of novel Z-scheme nitrogen-doped carbon dots/{001} TiO2nanosheetphotocatalysts for broad-spectrum-driven diclofenac degradation: mechanism insight, products and effects of natural water matrices, Chem. Eng. J. 356 (2019) 857–868, https://doi.org/10.1016/j.cej.2018.09.092.

[39] J. Liu, W. Zhu, S. Yu, X. Yan, Three dimensional carbogenic dots/TiO2 nanoheterojunctions with enhanced visible light-driven photocatalytic activity, Carbon. 79 (2014) 369–379, https://doi.org/10.1016/j.carbon.2014.07.079.

[40] J. Di, J. Xia, M. Ji, B. Wang, S. Yin, Q. Zhang, Z. Chen, H. Li, Carbon quantum dots modified BiOCl ultrathin nanosheets with enhanced molecular oxygen activation ability for broad spectrum photocatalytic properties and mechanism insight, Acs Appl. Mater. Inter. 7 (2015) 20111–20123, https://doi.org/10.1021/acsami.5b05268.

[41] A. Mewada, S. Pandey, S. Shinde, N. Mishra, G. Oza, M. Thakur, M. Sharon, M. Sharon, Green synthesis of biocompatible carbon dots using aqueous extract of Trapabispinosa peel, Mater. Sci. Eng. C-Mater. 33 (2013) 2914–2917, https://doi.org/10.1016/j.msec.2013.03.018.

[42] W. Shi, X. Zhang, J. Brillet, D. Huang, M. Li, M. Wang, Y. Shen, Significant enhancement of the photoelectrochemical activity of WO3 nanoflakes by carbon quantum dots decoration, Carbon. 105 (2016) 387–393, https://doi.org/10.1016/j.carbon.2016.04.051.

[43] H. Ming, Z. Ma, Y. Liu, K. Pan, H. Yu, F. Wang, Z. Kang, Large scale electrochemical synthesis of high quality carbon nanodots and their photocatalytic property, Dalton Trans. 41 (2012) 9526–9531, https://doi.org/10.1039/c2dt30985h.

[44] S. Qu, X. Wang, Q. Lu, X. Liu, L. Wang, A biocompatible fluorescent ink based on water-soluble luminescent carbon nanodots, Angew. Chem. Inter. Ed. 51 (2012) 12215–12218, https://doi.org/10.1002/anie.201206791.

[45] X. Yu, J. Liu, Y. Yu, S. Zuo, B. Li, Preparation and visible light photocatalytic activity of carbon quantum dots/TiO2 nanosheet composites, Carbon. 68 (2014) 718–724, https://doi.org/10.1016/j.carbon.2013.11.053.

[46] T.M. Perfecto, C.A. Zito, T. Mazon, D.P. Volanti, Flexible room-temperature volatile organic compound sensors based on reduced graphene oxide-WO3 center dot 0.33H2O nano-needles, J. Mater. Chem. C Mater. Opt. Electron. Devices 6 (2018) 2822–2829, https://doi.org/10.1039/c8tc00324f.

[47] L. Yang, Y. Liu, R. Zhang, W. Li, P. Li, X. Wang, Y. Zhou, Enhanced visible-light photocatalytic performance of a monolithic tungsten oxide/graphene oxide aerogel for nitric oxide oxidation, Chin. J. Catal. 39 (2018) 646–653, https://doi.org/10.1016/S1872-2067(17)62974-7.

[48] J. Ke, H. Zhou, J. Liu, X. Duan, H. Zhang, S. Liu, S. Wang, Crystal transformation of 2D tungstic acid H2WO4 to WO3 for enhanced photocatalytic water oxidation, J. Colloid Interf. Sci. 514 (2018) 576–583, https://doi.org/10.1016/j.jcis.2017.12.066.

[49] G. Xi, S. Ouyang, P. Li, J. Ye, Q. Ma, N. Su, H. Bai, C. Wang, Ultrathin W18O49nanowires with diameters below 1 nm: synthesis, near-infrared absorption, photoluminescence, and photochemical reduction of carbon dioxide, Angew. Chem. Int. Ed. English 51 (2012) 2395–2399, https://doi.org/10.1002/anie.201107681.

[50] J. Tong, L. Bo, X. Cai, H. Wang, Q. Zhang, L. Su, Aerobic oxidation of cyclohexane effectively catalyzed by simply synthesized silica-supported cobalt ferrite magnetic nanocrystal, Ind. Eng. Chem. Res. 53 (2014) 10294–10300, https://doi.org/10.1021/ie5008213.

[51] W. Wu, Z. Fu, S. Tang, S. Zou, X. Wen, Y. Meng, S. Sun, J. Deng, Y. Liu, D. Yin, (nBu4N)4W10O32-catalyzed selective oxygenation of cyclohexane by molecular oxygen under visible light irradiation, Appl. Catal. B-Environ. 164 (2015) 113–115, https://doi.org/10.1016/j.apcatb.2014.08.045.

[52] Y. Ide, M. Iwata, Y. Yagenji, N. Tsunoji, M. Sohmiya, K. Komaguchi, T. Sanoc, Y. Sugahara, Fe oxide nanoparticles/Ti-modified mesoporous silica as a photocatalyst for efficient and selective cyclohexane conversion with O2 and solar light, J. Mater. Chem. A Mater. Energy Sustain. 4 (2016) 15829–15835, https://doi.org/10.1039/c6ta04222h.

[53] X. Zhao, Y. Zhang, P. Wen, G. Xu, D. Ma, P. Qiu, NH2-MIL-125(Ti)/TiO2 composites as superior visible-light photocatalystsfor selective oxidation of cyclohexane, Mol. Catal. 452 (2018) 175–183, https://doi.org/10.1016/j.mcat.2018.04.004.

[54] J. She, J. Lin, Z. Fu, J. Li, S. Tang, M. Lei, X. Zhang, C. Zhang, D. Yin, HCl and O2 co-activated bi(8-quinolinolato) oxovanadium(IV) complexes as efficient photoactive species for visible light-driven oxidation of cyclohexane to KA oil, Catal. Sci. Technol. 9 (2019) 275–285, https://doi.org/10.1039/c8cy01241e.

[55] L. Xiang, J. Fan, W. Zhong, L. Mao, K. You, D. Yin, Heteroatom-induced band-

reconstruction of metal vanadates for photocatalytic cyclohexane oxidation towards KA-oil selectivity, Appl. Catal. A-Gen. 575 (2019) 120–131, https://doi.org/10.1016/j.apcata.2019.02.015.

[56] Y. Wan, Q. Guo, K. Wang, X. Wang, Efficient and selective photocatalytic oxidation of cyclohexane using O_2 as oxidant in $VOCl_2$ solution and mechanism insight, Chem. Eng. Sci. 203 (2019) 163–172, https://doi.org/10.1016/j.ces.2019.03.079.

[57] Z. Liang, J. Wei, X. Wang, Y. Yu, F. Xiao, Elegant Z-scheme-dictated g-C_3N_4 en-wrapped WO_3 superstructures: a multifarious platform for versatile photoredox catalysis, J. Mater. Chem. A Mater. Energy Sustain. 5 (2017) 15601–15612, https://doi.org/10.1039/c7ta04333c.

[58] B. Lin, Z. Lin, S. Chen, M. Yu, W. Li, Q. Gao, M. Dong, Q. Shao, S. Wu, T. Ding,

Z. Guo, Surface intercalated spherical $MoS_{2x}Se_{2(1-x)}$ nanocatalysts for highly efficient and durable hydrogen evolution reactions, Dalton Trans. 48 (2019) 8279–8287, https://doi.org/10.1039/c9dt01218d.

[59] J. Fu, Q. Xu, J. Low, C. Jiang, J. Yu, Ultrathin 2D/2D WO_3/g-C_3N_4 step-scheme H_2 production photocatalyst, Appl. Catal. B-Environ. 243 (2019) 556–565, https://doi.org/10.1016/j.apcatb.2018.11.011.

[60] W. Kong, X. Zhang, S. Liu, Y. Zhou, B. Chang, S. Zhang, H. Fan, B. Yang, N doped carbon dot modified WO_3 nanoflakes for efficient photoelectrochemical water oxidation, Adv. Mater. Inter. 6 (2019) 18016531, https://doi.org/10.1002/admi.201801653.